Journal of Catalysis 360 (2018) 66–80

Contents lists available at ScienceDirect

Journal of Catalysis

journal homepage: www.elsevier.com/locate/jcat

Selective conversion of acetone to isobutene and acetic acid on aluminosilicates: Kinetic coupling between acid-catalyzed and radical-mediated pathways

Stanley Herrmann, Enrique Iglesia *

Department of Chemical and Biomolecular Engineering, University of California, Berkeley, United States

ARTICLE INFO

Article history:
Received 1 December 2017
Revised 25 January 2018
Accepted 29 January 2018

Keywords:
Solid Brønsted acids
Aldol condensation
β-Scission in oxygenates
Radical chain cycles
Confinement effects

ABSTRACT

Solid Brønsted acids catalyze aldol condensations that form C—C bonds and remove O-atoms from oxygenate reactants, but sequential β-scission reactions also cleave C—C bonds, leading to isobutene and acetic acid products for acetone reactants. The elementary steps and site requirements that cause these selectivities to depend sensitively on Al content and framework type in aluminosilicate solid acids remain speculative. Acetone reactions on microporous and mesoporous aluminosilicates (FER, TON, MFI, BEA, MCM-41) showed highest β-scission selectivities on MFI and BEA; they increased as the Al content and the intracrystalline density of active protons decreased. The effects of acetone and H_2O pressure on turnover rates and selectivities indicate that an equilibrated pool of reactive C_6 ketols and alkenones are present at pseudo-steady-state concentrations during catalysis and that they act as intermediates in β-scission routes. Two distinct C_6 β-scission pathways contribute to the formation of isobutene and acetic acid: (i) a minor H_2O-mediated route involving β-scission of C_6 ketols on protons and (ii) the predominant anhydrous path, in which H-transfer forms unsaturated C_6 enols at protons and these enols propagate radical chains mediated by transition states stabilized by van der Waals contacts within vicinal microporous voids. This latter route is consistent with coupled-cluster free energy estimates for these unsaturated C_6 enols and their respective free radicals. It accounts for β-scission selectivities that increase with decreasing proton density, a finding that precludes the sole involvement of acid sites and requires instead the kinetic coupling between reactions at protons and propagation steps mediated by transition states confined within proximate voids, even when such voids lack a specific binding site. These mechanistic interpretations also account for the observed effects of residence time, of the loss of active protons by deactivation, of acetone and H_2O pressures, and of aluminosilicate framework structure on selectivity. These mechanistic insights also demonstrate the ability of voids to stabilize transition states that mediate homogeneous reactions by mere confinement, even in the absence of chemical binding onto specific sites, as well as the essential requirement of intimate proximity for the effective kinetic coupling between reactions on protons and in proton-free voids, a process mediated by the diffusion of very reactive and unstable intermediates present at very low local concentrations within microporous frameworks.

1. Introduction

The selective conversion of biomass-derived oxygenates to branched alkenes provides a route to useful chemicals from renewable sources [1–3]. One such pathway converts acetone, often formed from biomass fermentation or pyrolysis processes, to isobutene, a monomer widely used in the synthesis of butyl rubber and polyisobutylene [4,5], and to acetic acid, a co-product that can be converted to alkanones via ketonization [6–8]. This reaction occurs on solid acids, whether based on mesoporous oxides (silica-alumina, silica-tungstenate, silica-phosphoric acid) or on crystalline microporous aluminosilicates (MFI, BEA, ERI, FAU zeolites) [9–15]. Mechanistic details remain unclear because of concurrent and sequential oligomerization, ketonization, and isomerization reactions [16,17], which consume primary products and can form larger deactivating residues at the temperatures required for practical reactivity (550–600 K) [12,18]. Such mechanistic inquiries may allow the more precise tuning of selectivity to increase isobutene and acetic acid yields through more thoughtful choice of solid acids that provide specific confining void or proton densities.

---

* Corresponding author.
E-mail address: iglesia@berkeley.edu (E. Iglesia).

https://doi.org/10.1016/j.jcat.2018.01.032
0021-9517/Published by Elsevier Inc.

Alkanones form β-ketol dimers via aldol condensation on Brønsted acid sites at near-ambient temperatures [19]. These β-ketol species subsequently dehydrate on such acid sites to form α,β-unsaturated alkanones [20,21]. Alkenes can form via C—C bond cleavage of either the β-ketol species or their α,β-unsaturated alkanone products. The conversion of diacetone alcohol and mesityl oxide, the products of acetone condensation, into isobutene was first reported in 1940 by McAllister, et al. on silica-supported phosphoric acid catalysts [22]. Later studies on zeolitic acids have led to conflicting proposals about (i) the identity of the direct precursor to isobutene and acetic acid (mesityl oxide, diacetone alcohol, trimer oxygenate products, or larger unsaturated residues) [12–15]; (ii) the nature of the active sites (Brønsted or Lewis acid centers) [15,23]; (iii) the mechanistic role of water in determining isobutene selectivity and deactivation rates [12,23]; and (iv) the effect of Si/Al ratio in aluminosilicates on reactivity and isobutene selectivity [12,13,15,24].

These mechanistic and practical issues are addressed here through measurements of condensation turnover rates and isobutene selectivities on aluminosilicates with diverse framework structures (FER, TON, MFI, BEA, MCM-41) and with a range of proton and Al densities. These reactions are shown to occur via elementary steps that combine those involved in the formation of condensation products, previously established through kinetic, isotopic, spectroscopic, and theoretical tools [18], and those that mediate the conversion of an equilibrated pool of C_6 species to isobutene and acetic acid via two distinct routes; these routes involve an acid-catalyzed and a radical-mediated route, with the species that mediate the latter route formed initially on Brønsted acid sites. Condensation is limited by the C—C bond formation step on protons nearly saturated with H-bonded acetone, without detectable involvement of Lewis acid sites. Condensation rates thus reflect the preferential stabilization of the C—C bond formation transition state over H-bonded acetone precursors via van der Waals interactions with the confining framework voids when compared across aluminosilicates of similar acid strength [18]. These steps lead to rates (r_{cond}) that are proportional to acetone pressure (Ac) and to the number of accessible protons:

$$\frac{r_{\text{cond}}}{[H^+]} = k_{\text{cond}}(\text{Ac}) \quad (1)$$

with k_{cond} as the first-order condensation rate constant.

This study shows that isobutene and acetic acid form by reactions of an equilibrated pool of β-ketols and α,β-unsaturated alkanones (C_6-pool; Scheme 1), without the involvement of larger chains, as also shown in one previous study, in which isobutene with only one or three ^{13}C-atoms formed from ^{13}C-acetone–^{12}C-acetone mixtures on MFI and BEA [11]. The addition of H_2O on MFI samples with different proton density shows here that isobutene forms via two distinct routes that differ in the involvement of H_2O denoted here as anhydrous and H_2O-mediated β-scission routes. H_2O-mediated routes require only protons and occur at rates strictly proportional to their number for a given void structure and independent of the presence of non-framework Al species that may act as Lewis acids. These H_2O-mediated pathways are likely to involve diacetone alcohol β-scission (β_{DA} pathway), but kinetic data can only ascertain that this is the stoichiometry of the relevant transition state; thus, the hydrolytic cleavage of mesityl oxide may also contribute to such routes. The anhydrous routes, in contrast, involve the β-scission of species with the stoichiometry of mesityl oxide (β_{MO} pathway). These anhydrous pathways are much more prevalent than the H_2O-mediated route and lead to isobutene selectivities that increase, in an unusual and unexpected manner, as the proton density decreases, an observation reported, but not explained, in some previous studies [12,13,24]. These trends reflect pathways that require the presence of small voids acting in concert with protons. Protons isomerize mesityl oxide into unstable reactive intermediates that participate in radical propagation cycles mediated by transition states stabilized by van der Waals contacts with the walls of the confining voids, but without the involvement of specific binding sites.

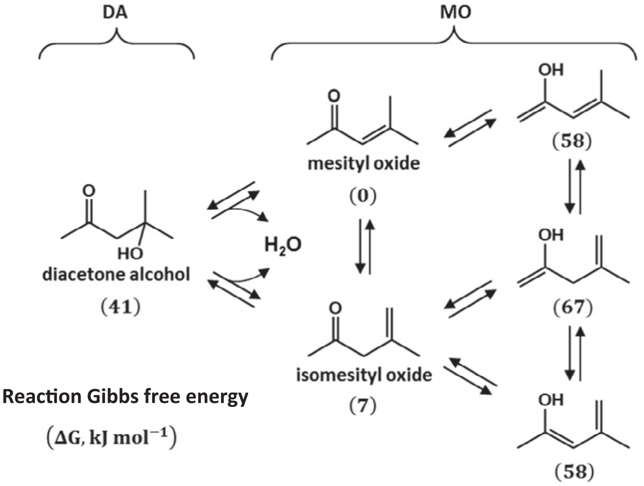

Scheme 1. Reaction network and Gibbs free energies (relative to mesityl oxide) for all gaseous C_6 species. Gibbs free energy differences between gaseous species and gaseous mesityl oxide molecules are provided in parenthesis (473 K, CCSD, AUG-cc-pVDZ; details in Section 2.3). The value for diacetone alcohol is the free energy difference between diacetone alcohol and the sum of mesityl oxide and H_2O in their gaseous states.

These synergistic effects of protons and small voids for β_{MO} routes cannot be reconciled with elementary steps that involve bifunctional catalysis (two distinct binding sites), or with non-framework Al acting as Lewis acid centers or silanols as weak Brønsted acids. Radical-like pathways enhanced by confinement and requiring nearby protons to replenish unstable compositional isomers of mesityl oxide that propagate radical chains are consistent with all data at hand. These routes resemble those that mediate gas phase decomposition of MO at higher temperatures (685–763 K) [25]; these homogeneous rearrangements are initiated by MO conversion to reactive alkenol isomers, which occurs, in this case, via facile hydride shifts at protons [26]. Confining voids in microporous acids (FER, TON, MFI, BEA) can decrease activation barriers, without the involvement of specific binding sites, as shown previously for other homogeneous reactions, such as NO oxidation [27] and diene cyclodimerization [28]. These previously unrecognized routes for β-scission of acetone-derived C_6 species involve intimate kinetic coupling between proton-catalyzed isomerization and radical-mediated β-scission propagation cycles, a mechanistic conclusion supported by free energy estimates for C_6 intermediates and their respective radicals. These theoretical treatments suggest that these free-radical mediated β-scission pathways, made possible by protons and confining voids within nanometer distances, represent the only plausible mechanism consistent with rate and selectivity data for the anhydrous β-scission routes that prevail at practical conditions for the conversion of acetone to isobutene and acetic acid.

2. Methods

2.1. Catalyst synthesis and characterization protocols

NH_4-MFI (Zeolyst, Si/Al$_{\text{tot}}$ = 16.6, 29.2, 43.8, and 168.3), NH_4-BEA (Zeolyst, Si/Al$_{\text{tot}}$ = 43.3), NH_4-FER (Zeolyst, Si/Al$_{\text{tot}}$ = 10.3), NH_4-TON (BP p.l.c., Si/Al$_{\text{tot}}$ = 40.0), and NH_4-MCM-41 (Sigma-Aldrich, 643,653, Si/Al$_{\text{tot}}$ = 37.8) were treated in flowing dry air

($1.5\ cm^3\ g^{-1}\ s^{-1}$, zero grade, Praxair) heated to 823 K (at 0.025 K s^{-1}) and held for 5 h. Their Si, Al, and Na contents were measured by inductively-coupled plasma atomic emission spectroscopy (ICP-AES; Galbraith Laboratories). Table 1 lists the nomenclature used to denote each sample together with their provenance, Si/Al and H^+/Al ratios, and proton density. The void structures (Table 1) are described by two size metrics: (i) the largest inscribed sphere (largest cavity diameter) and (ii) the largest sphere that can traverse each framework (pore-limiting diameter); both metrics are derived from crystallographic data [29].

SIL-1 (silicate-1, pure silica MFI) samples were prepared [27] by adding fumed SiO_2 (Cabosil M5) to a solution of tetrapropylammonium hydroxide (TPAOH; Alfa Aesar, 40% wt.) and stirring for 2 h. Aqueous HF was then added (Alfa Aesar, 48% wt.) and the suspension was stirred for 4 h. The resulting gel (1 SiO_2/0.1 TPAOH/ 0.1 HF/33 H_2O molar ratios; pH = 5.5) was placed within a Teflon-lined stainless-steel autoclave (Parr; 23 cm^3), heated to 448 K under autogenous pressure, and held for 14 days without stirring. The resulting suspension was cooled to ambient temperature and filtered to recover the solids. These solids were washed with deionized H_2O (>17.6 Ω cm resistivity) until the pH of the filtrate was below 9, and then dried at ambient temperature in ambient air for 8 h. The solids were then heated to 823 K (at 0.05 K s^{-1}) in ambient air and held for 6 h to remove the TPAOH structure-directing agent. The SIL-1 structure was confirmed by X-ray diffraction (Philips X'pert diffractometer) using a Cu Kα source (5°–50°, 0.02° step size, 2 s hold).

2.2. Catalytic rate and selectivity measurements

Acetone conversion rates and selectivities were measured at low conversions (<6%) and 473 K. Catalyst powders were pressed into wafers (690 bar, 0.1 h), crushed, and sieved to retain 180–250 μm aggregates. Catalysts (0.020–0.200 g) were placed within a tubular quartz reactor (7.0 mm i.d.) and held at constant temperature using a three-zone resistively-heated furnace (Applied Test Systems Inc., model number 3210) and three temperature controllers (Watlow Series 988). Temperatures were measured with K-type thermocouples (Omega) and the reactor temperature was determined from a thermocouple placed in contact with the outer quartz tube surface at the catalyst bed midpoint. Catalysts (Table 1) were treated in flowing dry air ($83.3\ cm^3\ g^{-1}\ s^{-1}$, extra dry, Praxair) by heating to 818 K (at 0.025 K s^{-1}; 2 h hold) and subsequently cooled to reaction temperature before rate and selectivity measurements.

Liquid acetone (≥99.9%, Sigma-Aldrich) and deionized H_2O (>17.6 Ω cm resistivity) were introduced into He flow (UHP, Praxair) using syringe pumps (Legato 100, KD Scientific) and transfer lines held at 400 K. Inlet and effluent streams were analyzed by gas chromatography (GC; Agilent 6890A) using flame ionization detection (FID) after chromatographic separation (HP-1 column, Agilent). Molecular speciation was confirmed using mass spectrometry (MKS Spectra Minilab) and known standards. Retention times and response factors were determined from known concentrations of: acetone (≥99.9%, Sigma-Aldrich), diacetone alcohol (≥98%, Santa Cruz Biotechnology), mesityl oxide (98%, Spectrum Chemical), isobutene (99.0%, Praxair), acetic acid (≥99.99%, Sigma Aldrich), and 1,3,5-trimethylbenzene (98%, Sigma-Aldrich).

The initial product of acetone condensation, diacetone alcohol (DA), was not detected in the effluent because of its fast dehydration and favorable thermodynamics (Scheme 1) to form mesityl oxide and H_2O, which lead to equilibrium DA concentrations ($0.00035–5.6 \times 10^{-9}$ Pa DA) below chromatographic detection limits. Isomesityl oxide (Scheme 1) was detected at concentrations in equilibrium with mesityl oxide, as expected from facile hydride shifts at protons (Scheme 1). The plausible quasi-equilibration of the C_6-pool, containing C_6 alkenones and C_6 alkenols (Scheme 1), was estimated from free energy differences among these C_6 species using coupled cluster methods (details in Section 2.3; Scheme 1). Atomic coordinates of all converged C_6 species are provide in Section S1 of the Supporting Information.

2.3. Coupled-cluster treatments of gaseous stable intermediates and radical species

Electronic energies and vibrational frequencies of gaseous molecules and gaseous radicals were estimated using coupled-cluster methods with single and double substitutions from the Hartee-Fock determinant (CCSD) [34–37] and with Dunning's correlation-consistent, polarized valence, double-zeta basis sets [38–40] and added angular momentum diffuse functions (AUG-cc-pVDZ) [38,40] using the Gaussian 09 code [41]. Enthalpic and entropic corrections at reaction temperatures were determined from vibrational frequencies; these corrections together with electronic energies were used to calculate the Gibbs free energies of each species and their interconversion reactions (ΔG):

$$\Delta G = \sum_{p}^{\text{products}} G_p - \sum_{r}^{\text{reactants}} G_r \qquad (2)$$

Table 1
Zeolitic and mesoporous aluminosilicate samples.

Sample	Source	Si/Al ratio[a]	H^+/Al	H^+/unit cell[e]	d_{LCD}[f] (nm)	d_{PLD}[g] (nm)
MFI-1	Zeolyst	16.6	0.65[b]	3.56	0.70	0.50
MFI-2	Zeolyst	29.2	0.77[b]	2.45	0.70	0.50
MFI-3	Zeolyst	43.8	1.03[b]	2.20	0.70	0.50
MFI-4	Zeolyst	168.3	0.70[b]	0.41	0.70	0.50
BEA	Zeolyst	43.3	1.04[c]	1.50	0.69	0.67
FER	Zeolyst	9.5	0.35[b]	1.12	0.70	0.53
TON	[30,31]	40.0	0.88[d]	0.52	0.57	0.57
MCM-41	Sigma-Aldrich	37.8	0.42[c]	–	2.50[h]	2.50[h]

[a] Elemental analysis (ICP-AES; Galbraith Laboratories).
[b] From pyridine titrations during CH_3OH dehydration at 433 K [32].
[c] From 2,6-di-*tert*-butylpyridine titrations during acetone condensation at 473 K [18].
[d] From the amount of NH_3 evolved from NH_4^+-exchanged samples during thermal treatment [16].
[e] Proton density calculated using Si/Al and H^+/Al values reported here and unit cell parameters reported by the International Zeolite Association (IZA)[33]
[f] Largest-cavity diameter [29].
[g] Pore-limiting diameter [29].
[h] Pore diameter reported by commercial producer (Sigma-Aldrich).

where G_i represents the free energy of a reactant (r) or product (p). The free energies of all C_6 intermediates relative to MO are shown in Scheme 1.

Free energy differences between products and reactants were used to estimate equilibrium constants (K_{eq}) for reactions:

$$K_{eq} = \exp\left(-\frac{\Delta G}{k_B T}\right) \tag{3}$$

where k_B is the Boltzmann constant and T is the reaction temperature (K). These equilibrium constants, taken together with the measured pressures of reactant and product species ((X$_i$); $i = r$ or p, respectively; units: bar), are used to determine the approach to equilibrium (η) for each of these interconversion reactions:

$$\eta = \frac{1}{K_{eq}} \frac{\prod_p^{\text{products}}(X_p)}{\prod_r^{\text{reactants}}(X_r)} \tag{4}$$

3. Results and discussions

3.1. Effect of acetone pressure on catalyst deactivation rates and reaction selectivities

Aluminosilicates with different framework structures (FER, TON, MFI, BEA, MCM-41) and proton densities ($0.07–0.62H^+/g_{zeolite}$; Table 1) are used here to examine the elementary steps and site requirements for acetone conversion to isobutene (C_4) and acetic acid. Such mechanistic assessments and reactivity comparisons among samples and between theory and experiment require that we express reactivity in terms of rate constants rigorously normalized by the number of accessible protons. Rate and selectivity data on MFI-3 are reported in this section, as an illustrative example, to determine sequences of elementary steps consistent with the effects of acetone pressure and conversion on C_4 selectivity and on deactivation rates. The general mechanistic conclusions reached remain valid for MFI samples with other proton densities (Section 3.4) and for other aluminosilicate frameworks (Section 3.2).

Condensation rates on MFI-3 decreased with time on stream at all acetone pressures (0.33–3.75 kPa acetone; Fig. 1) even at very low conversions ($\leq$6%) and concomitantly low product concentrations along the catalyst bed. First-order rate constants extrapolated to initial times (k_{cond}, Eq. (1); per proton in fresh sample ($H^+|_{t=0}$)) did not depend on acetone pressure and resemble values reported on MFI samples stabilized against deactivation by H_2 and Pt/SiO$_2$ present as a physical mixture [18]. These effective k_{cond} values on monofunctional MFI-3 catalysts decreased more strongly with time as acetone pressures increased (Fig. 1); these effects, taken together with the curvature evident in Fig. 1, indicate that deactivation events must involve sequential reactions of primary condensation products even at such low conversions [42,43].

Acetone condensation formed equilibrated mixtures of mesityl oxide and isomesityl oxide (C_6 alkenone condensation products (MO); Scheme 1) and equimolar amounts of isobutene and acetic acid (β-scission products). The C_4/MO molar ratios in products increased linearly with acetone conversion (Fig. 2), consistent with sequential β-scission reactions of primary condensation products, either C_6 (equilibrated DA and MO, Scheme 1) or even larger oligomers formed via reactions of acetone with the equilibrated C_6 pool (Scheme 2). These C_4/MO ratios increased with decreasing acetone pressure (Fig. 2), apparently because of the different molecularity of the transition states for the steps that form C_4 and DA species.

These data show that acetone conversion, varied either through deactivation (Fig. 2) or through changes in residence time (open diamonds, Fig. 2), affects C_4/MO ratios in the same manner, indicating that either (i) condensation active sites (protons in concentration denoted as (L_1), Scheme 2) [18] also act as the β-scission sites or (ii) different sites (L_2, Scheme 2) are involved in β-scission, but L_1 and L_2 sites deactivate at identical rates, plausibly because of pore blockages that obstruct access to sites within a given intracrystalline region. Either possibility would lead to identical changes in selectivity with conversion, irrespective of how conversion was varied (through changes in the number of sites or the molar flow rates).

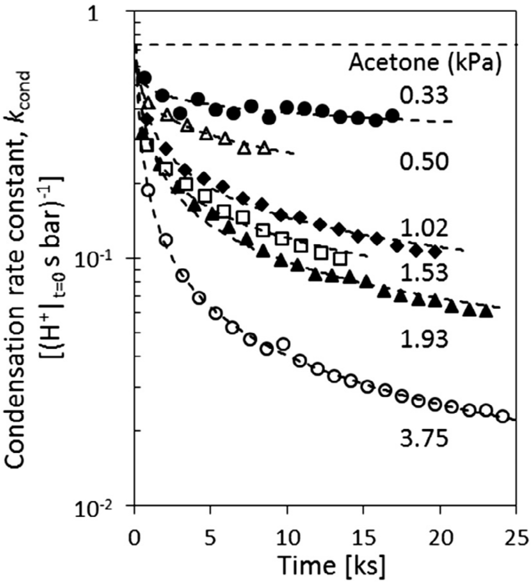

Fig. 1. Effective condensation rate constant per proton (k_{cond}; Eq. (1)) as a function of time-on-stream on MFI-3 at 0.33 (●), 0.50 (△), 1.02 (◆), 1.53 (□), 1.93 (▲), and 3.75 (○) kPa acetone (balance He, 473 K). Horizontal solid line represents first-order condensation rate constant on MFI stabilized with Pt and H_2 [18], and dashed curves represent trends.

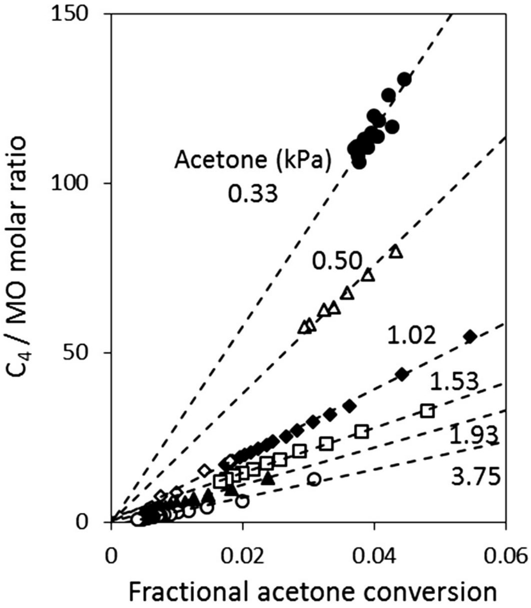

Fig. 2. Effect of acetone conversion on C_4/MO molar ratios on MFI-3 at 0.33 (●), 0.50 (△), 1.02 (◆,◇), 1.53 (□), 1.93 (▲), and 3.75 (○) kPa acetone (balance He, 473 K). Dashed lines are regressed linear fits of the data through the origin. Open diamonds are data points measured at different acetone residence times (6.6–15 (H^+·s) acetone^{-1}); all other data points are measured as conversion decreases while catalysts deactivate.

The measured C_4/MO product ratios (Fig. 2) were much larger than unity at all conditions, and the prevalent MO pressure in

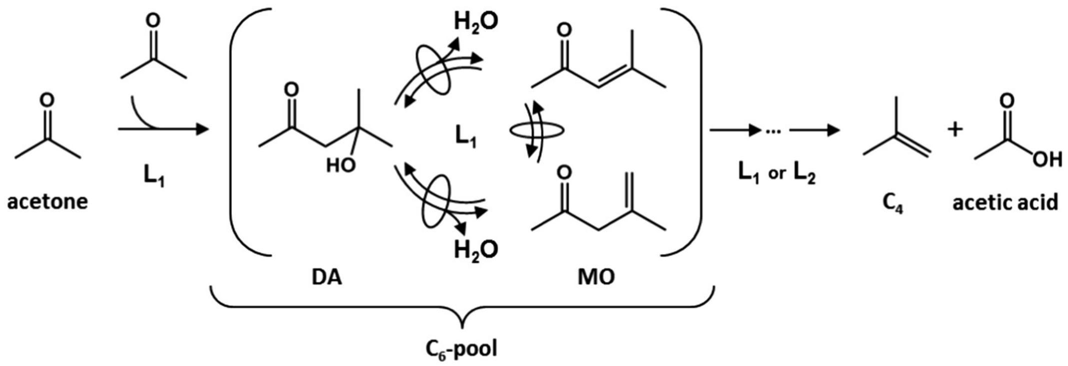

Scheme 2. Sequential reactions that mediate the formation of isobutene and acetic acid from acetone via β-scission routes on MFI. L_1 is a proton and L_2 is an active site different from a proton. An oval over double arrows denotes a quasi-equilibrated step.

the effluent stream was nearly independent of acetone conversion, as acetone conversion varied with deactivation or changes in residence time (Fig. 3a). These MO concentrations are proportional to the square of the acetone pressure (Fig. 3b). These data show that C_6 species undergo facile β-scission (Scheme 2) and that the concentrations of such species are set by either (i) equilibration with acetone reactants or (ii) steady-state concentrations set by the kinetic coupling of the steps that form and consume these C_6 molecules. Equilibration would not be consistent with condensation rates that are unaffected by the presence of H_2 and a Pt function, which lead to the rapid scavenging of MO and DA to form methyl isobutyl ketone, thus preventing both deactivation and β-scission, but without detectable consequences for initial condensation rates [18]. Indeed, CCSD calculations of free energies, required because thermodynamic data are not accurate for mesityl oxide, show that the approach to equilibrium (η; Eq. (4)) for the conversion of acetone to mesityl oxide (the most stable C_6 species; Scheme 1) and H_2O is <0.006 at all conditions, indicating that the concentrations of C_6 species are much lower than their equilibrium values for their formation from acetone.

Consequently, MO product concentrations must reflect pseudo-steady-state values given by the balance between the rates of C_6 formation and β-scission. C_6 species form via acetone condensation at rates (Scheme 2):

$$\frac{r_{formation}}{[H^+]} = \frac{k_{\mathrm{cond}} K_{Ac} (\mathrm{Ac})^2}{K_{Ac} (\mathrm{Ac})} \tag{5}$$

where k_{cond} and K_{Ac} are kinetic and thermodynamic constants for C—C bond formation and acetone adsorption on protons, respectively (Scheme 3, [18]). The denominator term, shown explicitly for clarity in Eq. (5), reflects nearly saturated coverages of H-bonded acetone present at protons, as shown by previous kinetic, spectroscopic, and theoretical studies [18,44,45].

The consumption of C_6 species is given by the molar rate of formation of C_4 products (or C_2 co-products) in the context of the sequential pathways shown in Scheme 2. C_4 species can form via β-scission of larger oligomers [14,15] or of C_6 species (β-ketol or α,β-unsaturated alkenones) [12–15,20,22]. These two routes (Scheme 2) combined give a rate equation with three additive rate terms:

$$\frac{r_{consumption}}{[H^+]} = \frac{\frac{k_{\beta,DA} K_{MO}}{K_{C_6}} (\mathrm{MO})(\mathrm{H_2O})}{K_{Ac}(\mathrm{Ac})} + \frac{k_{\beta,MO} K_{MO} (\mathrm{MO})}{K_{Ac}(\mathrm{Ac})} + \frac{k_{\mathrm{cond},C_9} (\mathrm{Ac}) K_{MO} (\mathrm{MO})}{K_{Ac}(\mathrm{Ac})} \tag{6}$$

which account for β-scission of diacetone alcohol (DA; C_6 β-ketol) and of MO and for acetone coupling with MO to form larger oligo-

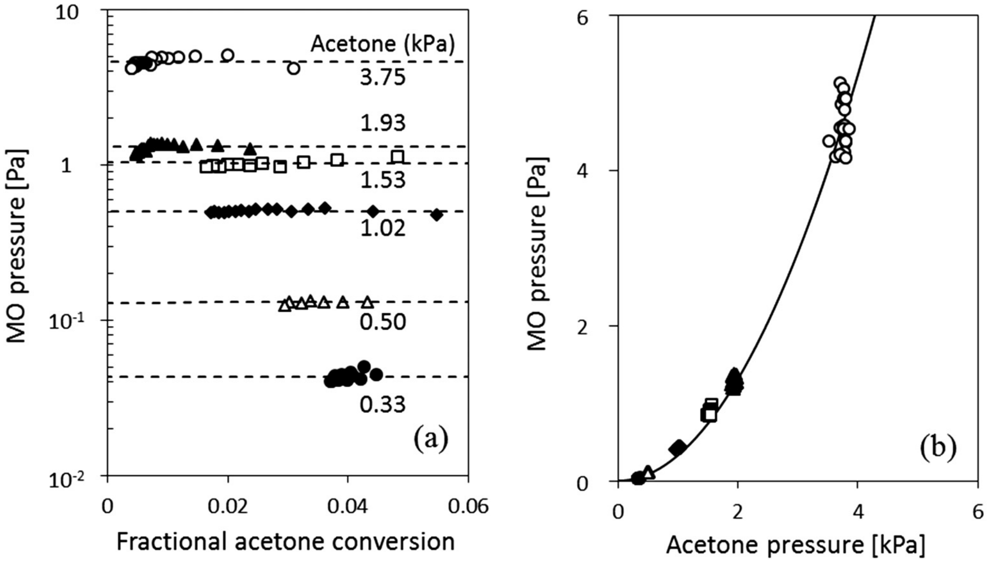

Fig. 3. MO pressure (lumped mesityl and isomesityl oxides, Scheme 1) as a function of (a) acetone conversion and (b) acetone pressure on MFI-3 at 0.33 (●), 0.50 (△), 1.02 (◆), 1.53 (□), 1.93 (▲), and 3.75 (○) kPa acetone (balance He, 473 K). Dashed lines represent regressed linear horizontal fits and solid curve represents regression of MO pressure to the functional form of Eq. (8).

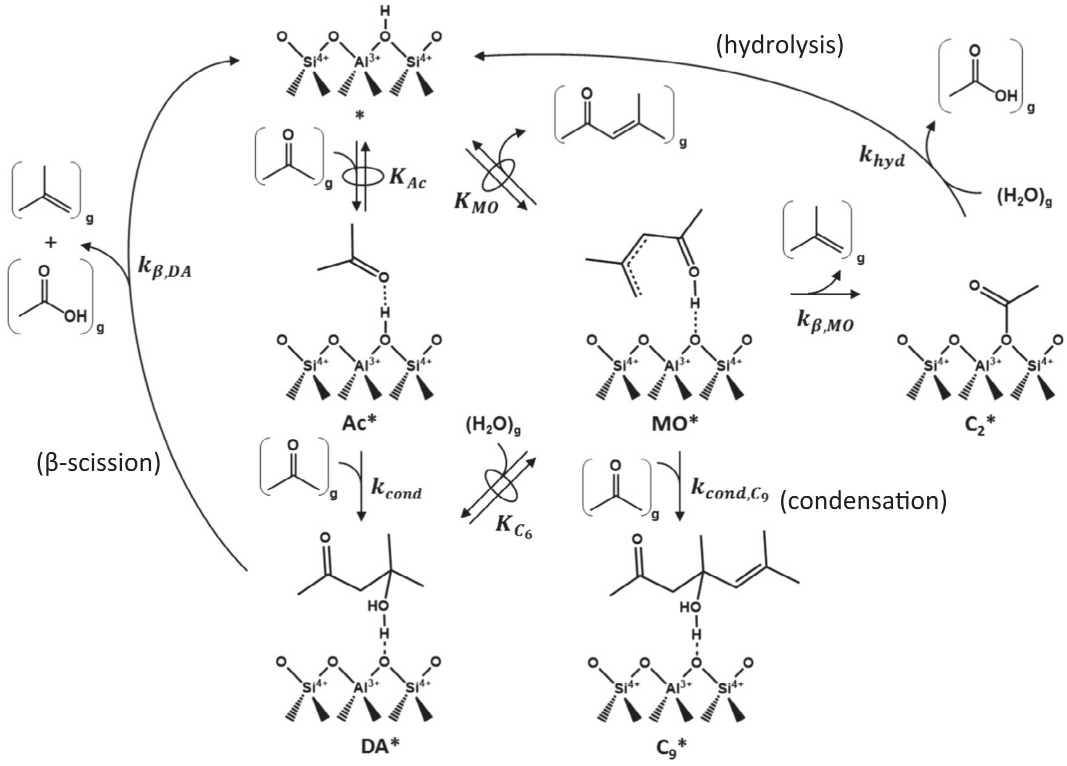

Scheme 3. Proposed elementary steps for the formation of MO, isobutene, and acetic acid from acetone reactions on Brønsted acid sites. Labels for bound intermediates correspond to bare protons (*), H-bonded acetone (Ac*), protonated diacetone alcohol (DA*), protonated mesityl oxide (MO*), acetates (C_2*), and protonated C_9 β-ketol species (C_9*). k_X and K_X denote kinetic constants for forward steps and equilibrium constants, respectively. Quasi-equilibrated steps are indicated by an oval over double arrows. Equilibrated double-bond isomers (Scheme 1) are indicated by dotted lines for double bonds.

mers; the k_X and K_X parameters are the kinetic and thermodynamic constants using the notation in Scheme 3 for each elementary step. The H_2O pressure equals the residual MO pressure, when larger oligomer formation is negligible, because any H_2O molecules formed in acetone condensation events are consumed when such products (MO or DA) undergo β-scission to form the predominant isobutene and acetic acid products (Scheme 3).

The pseudo-steady-state MO concentration is given by equating Eqs. (5) and (6):

$$(\mathrm{MO}) = \left(\frac{K_{C_6}}{2k_{\beta,DA}}\right)\left(\sqrt{\left(k_{\beta,MO} + k_{\mathrm{cond},C_9}(Ac)\right)^2 + 4\frac{k_{\beta,DA}}{K_{C_6}}\frac{k_{\mathrm{cond}}K_{Ac}}{K_{MO}}(\mathrm{Ac})^2} - \left(k_{\beta,MO} + k_{\mathrm{cond},C_9}(Ac)\right)\right) \tag{7}$$

The regression of all data in Fig. 3b to the functional form of this equation indicates that only the MO β-scission ($k_{\beta,MO}$) term is required to account for measured MO concentrations and for their $(\mathrm{Ac})^2$ dependence (Fig. 3b) without detectable contributions from DA β-scission $\left(k_{\beta,DA}K_{C_6}^{-1}\right)$ or MO-acetone coupling ($k_{\mathrm{cond},C_9}(\mathrm{Ac})$). As a result, Eq. (7) can be simplified to:

$$(\mathrm{MO}) = \frac{k_{cond}K_{Ac}}{k_{\beta,Mo}K_{MO}}(Ac)^2 \tag{8}$$

which accurately describes the effects of acetone pressure on MO concentrations measured on MFI-3 (Fig. 3b), but these acetone pressure effects (Eq. (8)) are also consistent with MO concentrations measured on all aluminosilicates used here (Section 3.2). Eq. (8) is also consistent with C_6 consumption via MO reactions mediated by transition states with the stoichiometry of MO, without additional H_2O moieties, and occurring on sites saturated with acetone-derived bound intermediates.

These effects of acetone pressure on the MO concentrations (Eq. (8)), taken together with Eq. (1), give C_4/MO selectivity ratios in agreement with the data in Fig. 2:

$$\frac{(\mathrm{C}_4)}{(\mathrm{MO})} = \frac{\frac{1}{2}X(\mathrm{Ac})}{\frac{k_{cond}K_{Ac}}{k_{\beta,MO}K_{MO}}(\mathrm{Ac})^2} = \frac{1}{2}\,\frac{k_{\beta,MO}K_{MO}}{k_{cond}K_{Ac}}\,\frac{X}{(\mathrm{Ac})} \tag{9}$$

which depend linearly on the ratio of the fractional acetone conversion (X) to the acetone pressure (Ac). This equation, derived from the assumption of pseudo-steady-state, remains valid at all conditions that lead to C_4/MO ratios significantly larger than unity (as observed experimentally) and provides insights into the chemical origins of the β_{MO} terms (the slope of C_4/MO ratios as a function of $X/(\mathrm{Ac})$; denoted as χ, Fig. 5):

$$\beta_{MO} \equiv \frac{k_{\beta,MO}K_{MO}}{k_{\mathrm{cond}}K_{Ac}} \tag{10}$$

Such kinetic analysis and the resulting β_{MO} values allow selectivity comparisons among aluminosilicates with different void environments or proton densities, all of which exhibit similar C_4 selectivity and acetone condensation kinetic dependences and condensation elementary steps similar to those shown above for MFI-3 and for FER, TON, MFI-(1-4), BEA, and MCM-41 catalysts in previous studies [18].

The first-order deactivation rate constants converged to a single curve for all acetone pressures (0.33–3.75 kPa, MFI-3, Fig. 4) when expressed as a function of the multiplicative product of MO pressure and time-on-stream. This trend is consistent with deactivation events mediated by sequential acetone condensation with C_6 species, which form larger oligomers that can block protons, thus preventing subsequent turnovers (Scheme 3) [18]. In such instances, condensation rates (r_{cond}; Eq. (1)) would decrease according to [46]:

$$r(t) = r_0 \cdot \exp(-k_d(\mathrm{MO})t) \tag{11}$$

where r_0 denotes the initial rate, t is time, and k_d is the deactivation rate constant (derivation in Supporting Information, S2). The data in Fig. 4 demonstrate the term (MO)t in the exponent of Eq. (11) in describing the acetone pressure effects on deactivation rates, but not with the curvature evident in Fig. 4. Such curvature, also shown in Fig. 1, indicates that the species that prevent condensation turnovers by strong binding onto protons also form from larger C_{9+} oligomers, via sequential processes not considered in the derivation of Eq. (11).

3.2. Effects of void environment on acetone conversion selectivity on solid acids

C_4/MO product ratios increased linearly with the value of χ (X/(Ac); Fig. 6) and all data lie along a single line for all acetone pressures (0.1–4 kPa acetone) on each of the aluminosilicate solid acids (MFI, BEA, TON, FER, MCM-41), indicative of common mechanistic underpinnings for these selectivities. On MFI, TON, and FER, MO species and β-scission products were the only products detected, but 1,3,5-trimethylbenzene (C_9) was also evident in the effluent stream for BEA and MCM-41 catalysts, which contain larger channels that allow the diffusion of these larger products (Table 1). C_9 products diffuse very slowly through the smaller channels in 10-member ring zeolites ($d_{PLD} \leq 0.57$ nm, MFI, TON, FER; Table 1), but egress more readily from 12-member ring zeolites (BEA, d_{PLD} = 0.67 nm) and from mesoporous aluminosilicates (MCM-41, d_{PLD} = 2.5 nm). C_9/MO product ratios on BEA and MCM-41 increased proportionally with χ-values (Fig. 6b), consistent with the formation of C_9 and C_4 products via secondary reactions of common intermediate products (C_6-pool) that occur after the kinetically-relevant C—C coupling step. Such kinetic branching of these C_6 intermediates leads to similar acetone pressure effects on C_9 and C_4 selectivities. The parallel nature of the pathways that convert C_6 species into C_4 and C_9 products, shown by their similar responses in selectivity to χ-values (Fig. 6a and b), is illustrated in Scheme 3.

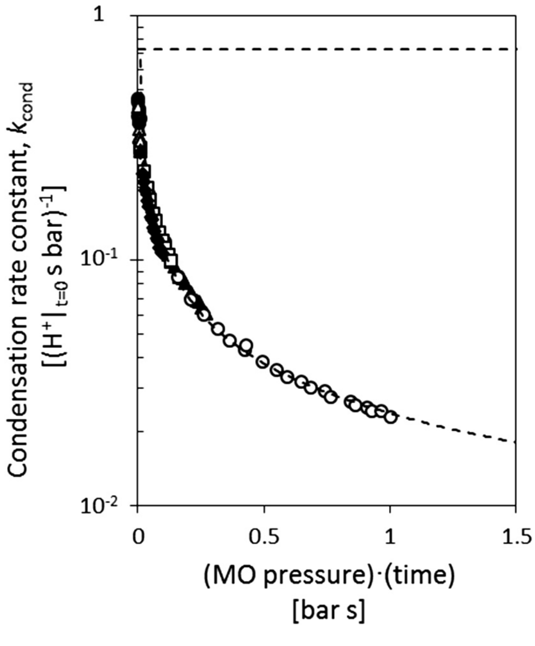

Fig. 4. Effective condensation rate constant (per proton) (k_{cond}; Eq. (1)) as a function of the product of time-on-stream and MO pressure. Rates on MFI-3 at 0.33 (●), 0.50 (△), 1.02 (◆), 1.53 (□), 1.93 (▲), and 3.75 (○) kPa acetone (balance He, 473 K). Horizontal solid line represents first-order condensation rate constant reported previously on Pt-stabilized MFI [18] and dashed curve represents the qualitative trends of the data.

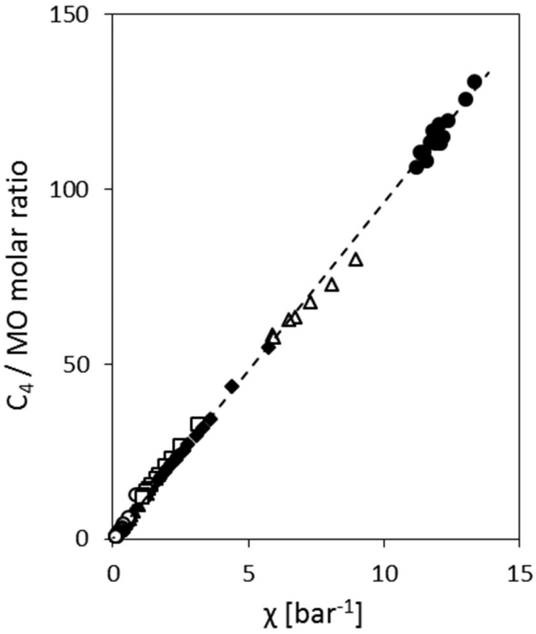

Fig. 5. Effect of acetone fractional conversion divided by acetone pressure (χ) on C_4/MO molar ratios measured on MFI-3 at 0.33 (●), 0.50 (△), 1.02 (◆), 1.53 (□), 1.93 (▲), and 3.75 (○) kPa acetone (balance He, 473 K). Dashed line is the regressed line through the origin.

The β_{MO} values, given by the slopes of the trends in Fig. 6a, reflect the ratio of rate constants for C_4 formation ($k_{\beta,MO}$, Eq. (10)) and acetone condensation (k_{cond}), while $k_{\beta,MO}$ describes the effectiveness of each catalyst in reactions that form isobutene and acetic acid via β-scission pathways. These $k_{\beta,MO}$ values (per proton) are shown in Fig. 7 for aluminosilicates with different void diameters (Table 1). These ($\beta_{MO} \cdot k_{cond}$)-values span a factor of nearly 10^3 and increase exponentially with increasing void size up to 0.7 nm (MFI and BEA, Table 1) and then decrease sharply for the larger voids in MCM-41. These trends in the effectiveness of host-guest interactions reflect van der Waals contacts between the framework and the confined organic moieties, which determine the stability of the cationic moiety at the β-scission transition states; such contacts are most effective for voids of ~0.7 nm diameter, an indication of the size of the relevant β-scission transition states.

The higher β-scission rate constants on MFI and BEA have led to previous reports [11–13,15,47] and patents [48,49] focusing on MFI as the preferred catalyst, but they remain without mechanistic explanations. Here, we examine the pathways involved in the secondary reactions that convert acetone to equimolar mixtures of isobutene and acetic acid using MFI and BEA as examples because of their high C_4 selectivities. These secondary reactions involve the conversion of molecules present as part of a quasi-equilibrated pool of C_6 species, within which the relative concentrations of the different components depend on the prevalent H_2O pressure (Scheme 2). The addition of H_2O, described in the next section, provides some additional insights into the specific involvement of these different components in β-scission reactions and in site blockage by secondary products, as well as compelling evidence for the involvement of parallel, and mechanistically distinct, anhydrous and H_2O-mediated β-scission pathways of C_6 intermediates.

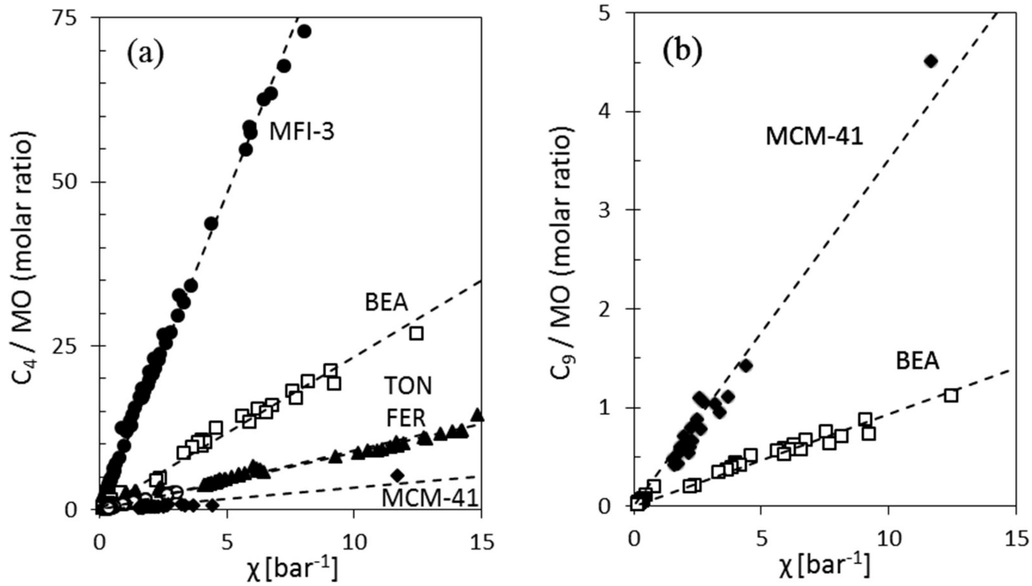

Fig. 6. (a) C_4/MO and (b) C_9/MO product molar ratios as a function of χ (acetone fractional conversion divided by acetone pressure) on aluminosilicates: MFI-3 (●), BEA (□), TON (▲), FER (○), and MCM-41 (◆) with different void structures (473 K, 0.1–4 kPa acetone). C_9 products were not detected on MFI-3, TON, or FER at these conditions. Dashed lines are regression fits of the data to the functional form of Eq. (9).

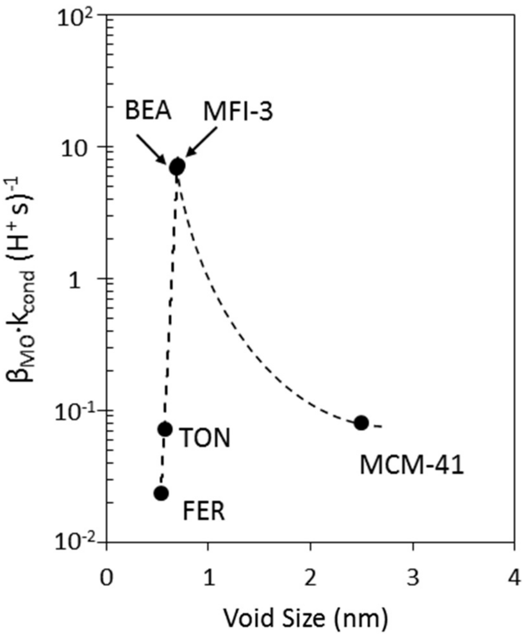

Fig. 7. Product of β_{MO} values (473 K, 0.1–4 kPa acetone; Eq. (10)) and first-order acetone condensation rate constants (k_{cond} from [18]) as a function of the void size in aluminosilicates (largest accessible cavity diameter; Table 1). β_{MO} and k_{cond} values for each aluminosilicate are listed in Table 2. Dashed lines represent trends.

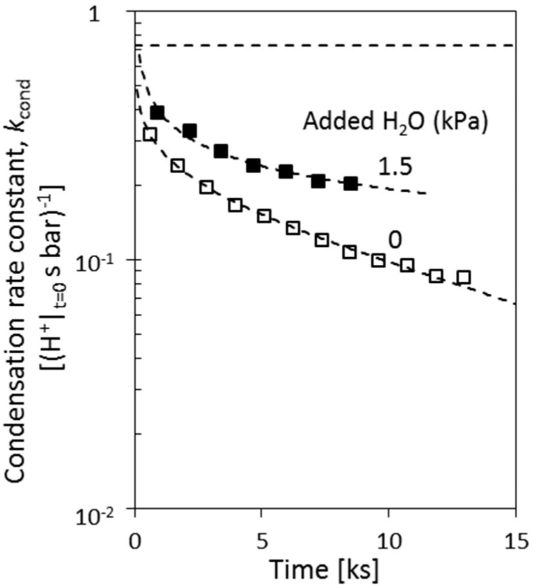

Fig. 8. Condensation rate constant (k_{cond}; Eq. (1)) as a function of time-on-stream. Rates were measured on MFI-3 (1.5 kPa acetone, 0 kPa H_2O added (□) or 1.5 kPa H_2O added (■), balance He, 473 K). Horizontal dashed line represents first-order condensation rate constant from ref [18] and dashed curves represent trends.

3.3. Effect of H_2O pressure on catalyst deactivation and product selectivity

Highly-reactive β-ketol species, such as DA, undergo facile dehydration to α,β- and β,γ-unsaturated alkanones on protons (Scheme 3); these unsaturated alkanones have been implicated as intermediates, without explicit mechanistic evidence, in deactivation rates and β-scission processes [12,23]. The addition of H_2O to acetone reactants led to slower deactivation (Fig. 8) and also to lower steady-state MO concentrations, thus increasing C_4/MO molar ratios (Fig. 9). Previous studies have shown that the H_2O/acetone molar ratios used in the present study (<3; Fig. 9) do not inhibit acetone condensation rates by competitive binding on protons [18]. These effects of H_2O on C_4/MO ratios (Fig. 9) indicate a shift in the equilibrated C_6 pool from alkenones to β-ketol species and, in the context of the mechanistic routes in Scheme 3, an increase in the rate of DA β-scission (the first term in Eq. (7)). The concomitant depletion of the C_6-pool by this additional conversion path leads, in turn, to lower rates of acetone reactions with this C_6-pool (Scheme 3) and thus to slower deactivation and higher C_4/MO ratios.

In the presence of added H_2O, any terms in Eq. (6) that depend on H_2O pressure cannot be neglected, thus Eq. (8) for the MO steady-state concentration becomes:

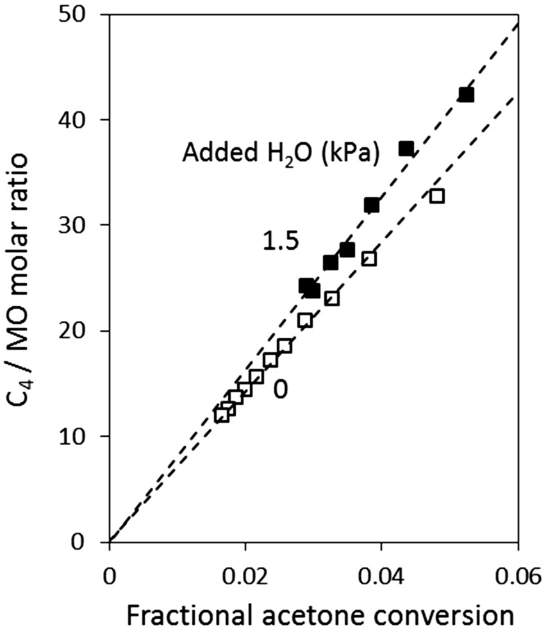

Fig. 9. Effect of acetone conversion on C_4/MO molar ratios on MFI-3 (1.5 kPa acetone, 0 kPa H_2O added (□) or 1.5 kPa H_2O added (■), balance He, 473 K). Dashed lines are regression fits of all data to a line passing through the origin.

$$(MO) = \frac{k_{cond}K_{Ac}(Ac)^2}{\frac{k_{\beta,DA}K_{MO}}{K_{C_6}}(H_2O) + k_{\beta,MO}K_{MO}} \tag{12}$$

which can be linearized to give:

$$\frac{(Ac)^2}{(MO)} = \frac{k_{\beta,DA}K_{MO}}{k_{cond}K_{Ac}K_{C_6}}(H_2O) + \frac{k_{\beta,MO}K_{MO}}{k_{cond}K_{Ac}} \tag{13}$$

consistent with the linear dependence of measured $(Ac)^2/(MO)$ ratios on H_2O pressure (Fig. 10). The two lumped parameters in Eq. (13) contain kinetic and thermodynamic constants for the elementary steps in Scheme 3. The asymptotic $(Ac)^2/(MO)$ ratio at low H_2O pressures (Eq. (13)) gives β_{MO} (Eq. (10)), while the slope of the data shown in Fig. 10 gives the corresponding constant for DA β-scission:

$$\beta_{DA} \equiv \frac{k_{\beta,DA}K_{MO}}{k_{cond}K_{Ac}K_{C_6}} \tag{14}$$

The data in Fig. 10 regressed to the form of Eq. (13) gives β_{DA} values of 260 ± 20 and 190 ± 40 for MFI-3 and BEA, respectively, and corresponding β_{MO} values of 24.5 ± 0.4 and 8.2 ± 0.9 bar (Table 2). These β_{MO} values reflect the considerable rates of C_4 formation during anhydrous acetone condensation reactions, where H_2O, formed during condensation, is required to form the isobutene and acetic acid β-scission products, but is not involved in the kinetically-relevant anhydrous β-scission transition state, consistent with the mechanistic conclusions presented in Section 3.1. This agreement between the data in Fig. 10 and the functional form of Eq. (13) suggests that DA β-scission contributes much less than MO β-scission to measured C_4 formation at low H_2O pressures; such findings are consistent with the low equilibrium concentrations of DA indicated by coupled cluster (CCSD, AUG-cc-pVDZ, 473 K) estimates of differences in free energies between gaseous MO (and H_2O) and DA (ΔG = +41 kJ mol^{-1}; Scheme 1).

These β_{DA} and β_{MO} values reflect free energy barriers (ΔG_X, where X = DA, MO) derived from transition state formalisms [50,51]:

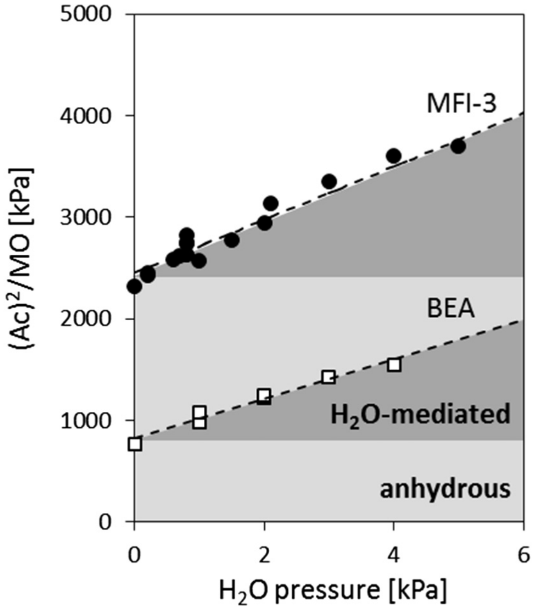

Fig. 10. Ratio of $(Ac)^2$ to MO as a function of H_2O pressure on MFI-3 (●) and BEA (□) (473 K, 0.5–2 kPa acetone). Dashed lines represent regressed linear fits of data to the form of Eq. (13), and the lighter and darker shaded regions denote contributions of MO β-scission (anhydrous) and DA β-scission (H_2O-mediated), respectively, to measured $(Ac)^2$/MO values.

$$k_X = \frac{k_BT}{h}\exp\left(-\frac{\Delta G_X}{k_BT}\right)\left(\frac{L_1}{L_i}\right) \tag{15}$$

where h is the Planck's constant, k_B is the Boltzmann constant, T is absolute temperature, and L_i is the number of active sites present for MO β-scission where i is 1 for protons or 2 for a different site (Scheme 2). The L_1/L_i ratio is present because Scheme 3 considers all reactions to occur on protons, while Eq. (15) retains the possibility that other sites, present at an amount L_i, may also be involved. In other words, rate constants (k_X) have been up to this point normalized by L_1 and this ratio allows the consideration of other active sites. The evidence for the existence of other plausible sites is presented in Sections 3.4 and 3.5. Eqs. (3) and (15) can be substituted into Eq. (10) for each of the kinetic and thermodynamic constants to give:

$$\beta_{MO} = \frac{k_{\beta,MO}K_{MO}}{k_{cond}K_{Ac}} = \frac{\left(\frac{L_1}{L_i}\right)\exp\left(-\frac{G^{\ddagger}_{\beta,MO}-(G_{MO}+G_{L_i})}{k_BT}\right)}{\exp\left(-\frac{G^{\ddagger}_{cond}-(2G_{Ac}+G_{L_1})}{k_BT}\right)} \tag{16}$$

The $G^{\ddagger}_j$ terms represent transition state free energies (subscripts are β, MO and cond for MO β-scission and acetone condensation); the G_h terms are the free energies of gaseous species ($h = MO$ and Ac for MO and acetone); G_{L_i} represents the free energy of the unoccupied sites (i = 1 or 2 for proton or a different site). Combining the exponent terms in Eq. (16) leads to:

$$\beta_{MO} = \left(\frac{L_1}{L_i}\right)\exp\left(-\frac{\Delta\Delta G_{\beta,MO}}{k_BT}\right) \tag{17}$$

with $\Delta\Delta G_{\beta,MO}$ defined as:

$$\Delta\Delta G_{\beta,MO} = \left(G^{\ddagger}_{\beta,MO} - (G_{MO} + G_{L_i})\right) - \left(G^{\ddagger}_{cond} - (2G_{Ac} + G_{L_1})\right) \tag{18}$$

and similarly, for β_{DA}:

$$\Delta\Delta G_{\beta,DA} = \left(G^{\ddagger}_{\beta,DA} - (G_{MO} + G_{H_2O} + G_{L_i})\right) - \left(G^{\ddagger}_{cond} - (2G_{Ac} + G_{L_1})\right) \tag{19}$$

Table 2
Acetone condensation rate constants (k_{cond}; Eq. (1)) and β-terms for MO (β_{MO}; Eq. (16) with L_i as the number of protons) and DA (β_{DA}; Eq. (14)) β-scission pathways.[a]

Sample	k_{cond}[b] $(H^+ \text{ s bar})^{-1}$	β_{MO}[c] bar	β_{MO}[d] bar	β_{DA}[d] a.u.
MFI-1	0.34 ± 0.06	8 ± 2	6 ± 2	240 ± 30
MFI-2	0.37 ± 0.02	12 ± 1	–	–
MFI-3	0.36 ± 0.04	20 ± 1	24.5 ± 0.4	260 ± 20
MFI-4	0.38 ± 0.02	74 ± 4	70 ± 6	280 ± 70
BEA	1.14 ± 0.04	6 ± 1	8.2 ± 0.9	190 ± 40
FER	0.013 ± 0.003	1.8 ± 0.3	–	–
TON	0.04 ± 0.02	1.8 ± 0.4	–	–
MCM-41	0.16 ± 0.01	0.50 ± 0.08	–	–

[a] Uncertainties represent 95% confidence interval for all regressed parameters.
[b] First-order acetone condensation rate constant from Ref. [18].
[c] β_{MO} from regression of C_4/MO ratios to the functional form of Eq. (10) (Fig. 6a and SI S.3).
[d] β_{MO} and β_{DA} determined by regression of $(Ac)^2$/MO ratios to the functional form of Eq. (13) (Figs. 9 and 11). Entries listed as "–" were not measured.

Eqs. (18) and (19) show the free energies that determine β_{MO} and β_{DA}; the respective equations differ in their different transition states for β-scission and in the presence of a term for the $H_2O(g)$ free energy (G_{H_2O}; present in Eq. (19)). These representations β_{MO} and β_{DA} can be substituted into Eq. (13) to give:

$$\frac{(Ac)^2}{(MO)} = (H_2O)\left(\frac{L_1}{L_{\beta,DA}}\right)\exp\left(-\frac{\Delta\Delta G_{\beta,DA}}{k_BT}\right) + \left(\frac{L_1}{L_{\beta,MO}}\right)\exp\left(-\frac{\Delta\Delta G_{\beta,MO}}{k_BT}\right) \qquad (20)$$

where $L_{\beta,DA}$ and $L_{\beta,MO}$ represent the number of active sites for the β-scission of DA and MO, respectively. Eq. (20) describes the response of MO concentration to potentially incorrect site normalizations in both β-scission pathways, which will be used in Section 3.4.

These mechanistic arguments and kinetic data indicate that β-scission can occur via parallel anhydrous and H_2O-mediated routes through transition states with the stoichiometry of MO and DA, respectively (Scheme 3). The additive contributions of H_2O-mediated routes lead to lower C_6 concentrations in the presence of added H_2O and to concomitant inhibition of deactivation events that involve condensation of acetone with C_6 species to form larger oligomers.

More detailed mechanistic assessments require that we consider the plausible presence of intracrystal concentration gradients of reactive C_6 species and the consequent diffusional enhancements of their secondary β-scission reactions; the resulting selectivities would then not merely reflect the rate and equilibrium constants of elementary steps at active sites. For each given framework, concentration gradients depend on the density of protons within aluminosilicate crystals, which set the formation rate of reactive intermediates (C_6), while the crystal size dictates the rates of their diffusional egress. C_4/MO product ratios on MFI with similar crystal sizes (75–150 nm) and different proton densities (0.41–3.56H^+/unit cell; Table 1) can be used to discern the presence and consequences of any diffusional limitations and to provide more detailed insights into the mechanism of β-scission, as discussed next.

3.4. Effects of MFI proton density on C_4/MO selectivity ratios

The values of the $(Ac)^2$/MO ratios on MFI-1, MFI-3, and MFI-4 increased linearly with H_2O pressure (Fig. 11) in a manner consistent with the functional form of Eq. (13). The resulting β_{DA} values (Eq. (14); Table 2) were similar on these MFI samples with tenfold differences in proton density (0.41–3.56H^+/unit cell, Table 1) and with similar crystal diameters (75–150 nm). These similar β_{DA} values and condensation rate constants (k_{cond} (per proton); Table 2) among MFI samples with different proton densities indicate that DA β-scission occurs solely on protons ($L_{\beta,DA} = L_1$; Eq. (20)) and that DA pressures are similar at all protons, which also shows that diffusion rates of C_6 species (DA and MO, equilibrated on protons) are sufficient to preclude intracrystalline C_6 concentration gradients. These latter findings are consistent with previous reports on these MFI samples at similar conditions, which led to the formation of only hydrogenated MO species (methyl isobutyl ketone, MIBK), without detectable β-scission, on physical mixtures of MFI and Pt/SiO_2 with added H_2 [18]. The absence of β-scission products in the presence of H_2 together with an extracrystalline Pt/SiO_2 function indicates that MO does not undergo β-scission as it egresses from MFI crystals; these data therefore confirm the absence of diffusional enhancements of secondary β-scission reactions as a result of the retention of MO and of any concomitant concentration gradients.

The β_{MO} values on MFI-1, MFI-3, and MFI-4 (Fig. 11; Table 2) monotonically increased as the density of protons decreased, an unexpected trend in the context of the mechanistic interpretation depicted as Scheme 3. The different β_{MO} values measured on MFI with different proton densities cannot be reconciled with reactions that occur solely on protons; these β_{MO} values are also not consis-

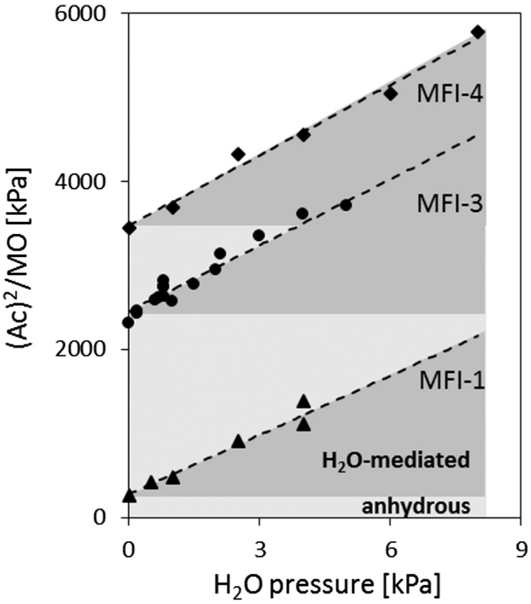

Fig. 11. Ratio of $(Ac)^2$ to MO as a function of H_2O pressure on MFI-1 (▲), MFI-3 (●), and MFI-4 (◆) (473 K, 0.5–2 kPa acetone). Dashed lines represent regressed linear fits of data to the form of Eq. (13), and the lighter and darker shaded regions denote contributions of the anhydrous and H_2O-mediated routes, respectively, to measured $(Ac)^2$/MO values.

tent with β-scission events involving non-framework Al sites (given by the deviations of H^+/Al values from unity; Table 1) or potential sites present after the catalyst bed that were ruled out by experiments on a MFI catalyst bed placed before a Pt/SiO_2 bed with added H_2 (27 kPa); such arrangements led to C_4 selectivities similar to those on the MFI bed alone (except for the formation of the hydrogenated form of products on the stacked beds). The similar condensation turnover rates among these MFI samples (Table 2) and the essential absence of β-scission during one crystal sojourn also rule out the presence of kinetically-consequential acetone or MO concentration gradients within crystals. Yet, β_{MO} values that increase with decreasing proton density must reflect a change in local pseudo-steady-state MO concentrations at intracrystalline protons; such dependences, as shown in Fig. 12 (lighter squares), suggest that the ratio of protons to sites relevant for MO β-scission ($L_1/L_{\beta,MO}$, Eq. (20)) is proportional to the proton density of the catalyst (H^+/unit cell), where the number of unit cells serves as a proxy for the microporous void volume with or without protons present. β_{MO} values, when calculated using proton density as the surrogate site ratio (Eq. (16)), are constant among MFI samples with different proton density (darker squares, Fig. 12) indicating that anhydrous β-scission depends on the number of protons and on the presence of microporous volume irrespective of whether such void volume actually contains a proton.

Similar β_{MO} values among MFI samples with different proton densities (darker squares, Fig. 12) suggests that anhydrous β-scission can occur within the microporous MFI voids, even when such voids lack a proton. Such a mechanism requires that $L_{\beta,MO}$ (L_i, Eq. (16)) represents the number of unit cells, a surrogate for microporous volume. This hypothesis was examined by using Al-free MFI samples (SIL-1), which did not, however, lead to detectable reactions of acetone (0.5–1.0 kPa, 473 K) or of MO/H_2O mixtures (0.02 kPa MO, 0–0.6 kPa H_2O, 473 K), thus, a proton is required for both acetone condensation and MO β-scission. These data confirm that voids alone cannot catalyze MO β-scission directly; thus, anhydrous β-scission reactions occurring within proton-free voids require MO-derived intermediates that form on protons within some diffusion distance of such voids.

The required presence of both protons and microporous volume was examined using physical mixtures of MFI-2 and SIL-1. These mixtures lead to C_4/MO molar ratios and β_{MO} values identical to those on MFI-2 (Fig. 13; β_{MO} = 30–31 bar·H^+·(MFI-2 unit cell)$^{-1}$). Thus, proton-free voids required (but not sufficient) for anhydrous β-scission routes need the presence of protons at distances much shorter than crystal diameters (75–150 nm), indicative of the involvement of unstable molecular shuttles that kinetically couple the events that occur on protons and within proton-free voids. This indicates, in turn, that MO β-scission routes do not involve direct reactions of mesityl oxide and isomesityl oxide, which are present at detectable concentrations even in the extracrystalline fluid phase and which would therefore benefit from the presence of SIL-1 in contact with such fluid phase. Pathways mediated by thermodynamically-unstable MO-derived enol-type species (Scheme 1) are left as the only plausible choice as intermediates in anhydrous MO β-scission reactions that form isobutene and acetic acid.

The effects of intracrystalline proton density on C_4/MO product ratios show that H_2O-mediated β-scission routes require protons, while anhydrous β-scission routes require protons and voids and thus depend on both the number of protons and the number of voids, even when such voids do not contain a proton (Fig. 12). Such "bifunctional" requirements are unique in that one of the two functions lacks a specific binding site and increases reaction rates by mere confinement through van der Waals contacts between the relevant transition state and the framework. Such confinement effects become possible only when protons reside beyond diffusion distances that can be traversed by highly-unstable MO-derived intermediates present at very low concentrations. These requirements may reflect radical-type reactions that are initiated at protons, but which propagate through long chains via reactions that benefit from confinement, even in the absence of a binding site. Next, we consider the nature of such possible radical-mediated pathways and the role of confinement in stabilizing the transition states for initiation steps and for propagation cycles.

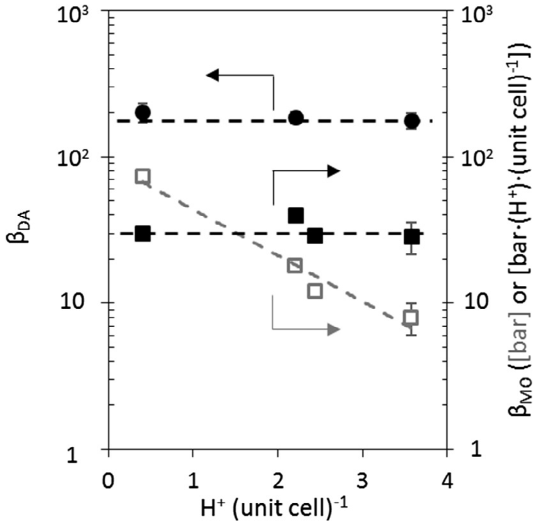

Fig. 12. DA β-scission reaction constants (β_{DA}, (●); Eq. (14); left ordinate) and MO β-scission rate constants (β_{MO}, (■, □); Eq. (16) with L_i as the number of unit cells or the number of protons represented, respectively, with darker closed squares or lighter open squares; right ordinate) as a function of the proton density in MFI (473 K, 0.5–2 kPa acetone, 0–7.5 kPa H_2O). Dashed horizontal lines represent the mean value for each parameter.

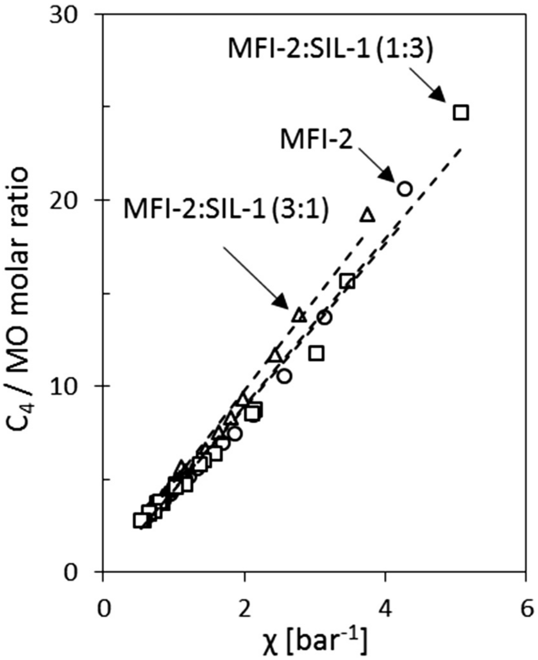

Fig. 13. Effect of dilution of MFI with SIL-1 on C_4/MO ratios at each value of χ (acetone conversion divided by acetone pressure) on MFI-2 (○), MFI-2 + SIL-1 (1:3 mass ratio; □), and MFI-2 + SIL-1 (3:1 mass ratio; Δ) (473 K, 1.0 kPa acetone). Dashed lines are regression fits of this data to the functional form of Eq. (9).

3.5. Implications of free radical β-scission of C_6 alkenone intermediates within confining voids

Radical-mediated chains that require protons to form unstable MO-derived intermediates (via hydride shifts to form C_6 alkenols) are examined here using theoretical treatments. These intermediates either decompose to initiate chains (Scheme 4a) or react with a radical-type species in propagation cycles (Scheme 4b) favored within confining voids; their intermediates, however, must be replenished via reactions of MO on protons, which are required for the hydride shifts that form the unstable alkenol species.

Radical-mediated homogeneous decomposition of alkanones occurs via homolytic cleavage of the C—C bond between the carbonyl and the α C-atoms [52,53], as illustrated for isomesityl oxide in Scheme 4a. Coupled cluster (CCSD) estimates of the free energy differences between gaseous isomesityl oxide and its gaseous radical products (allylic isobutenyl and acyl radicals, Scheme 4a) are +188 kJ mol^{-1} (CCSD, AUG-cc-pVDZ). This CCSD-estimate, taken together with DFT-estimates of the activation barrier for acetone condensation in MFI (120 kJ mol^{-1} (473 K), [18]) and the free energy difference between mesityl oxide and isomesityl oxide (7 kJ mol^{-1}, Scheme 1), indicates that the gaseous decomposition of isomesityl oxide would give a $\Delta\Delta G_{\beta,MO}$ value of +75 kJ mol^{-1} (Eq. (18)) and β_{MO} values of 5.2×10^{-9} bar·H$^+$·(unit cell)$^{-1}$ (Eq. (17)). Such a large barrier renders purely homogeneous routes inconsistent with the β_{MO} values measured here (31 ± 3 bar·H$^+$·(unit cell)$^{-1}$, MFI; Fig. 12). These barriers may, however, decrease upon confinement of such transition states within proton-free voids, but the stabilization free energies required to reach agreement with the measured β_{MO} values ($\Delta\Delta G_{\beta,MO} = -11 \pm 10$ kJ mol^{-1}; 473 K; Eq.

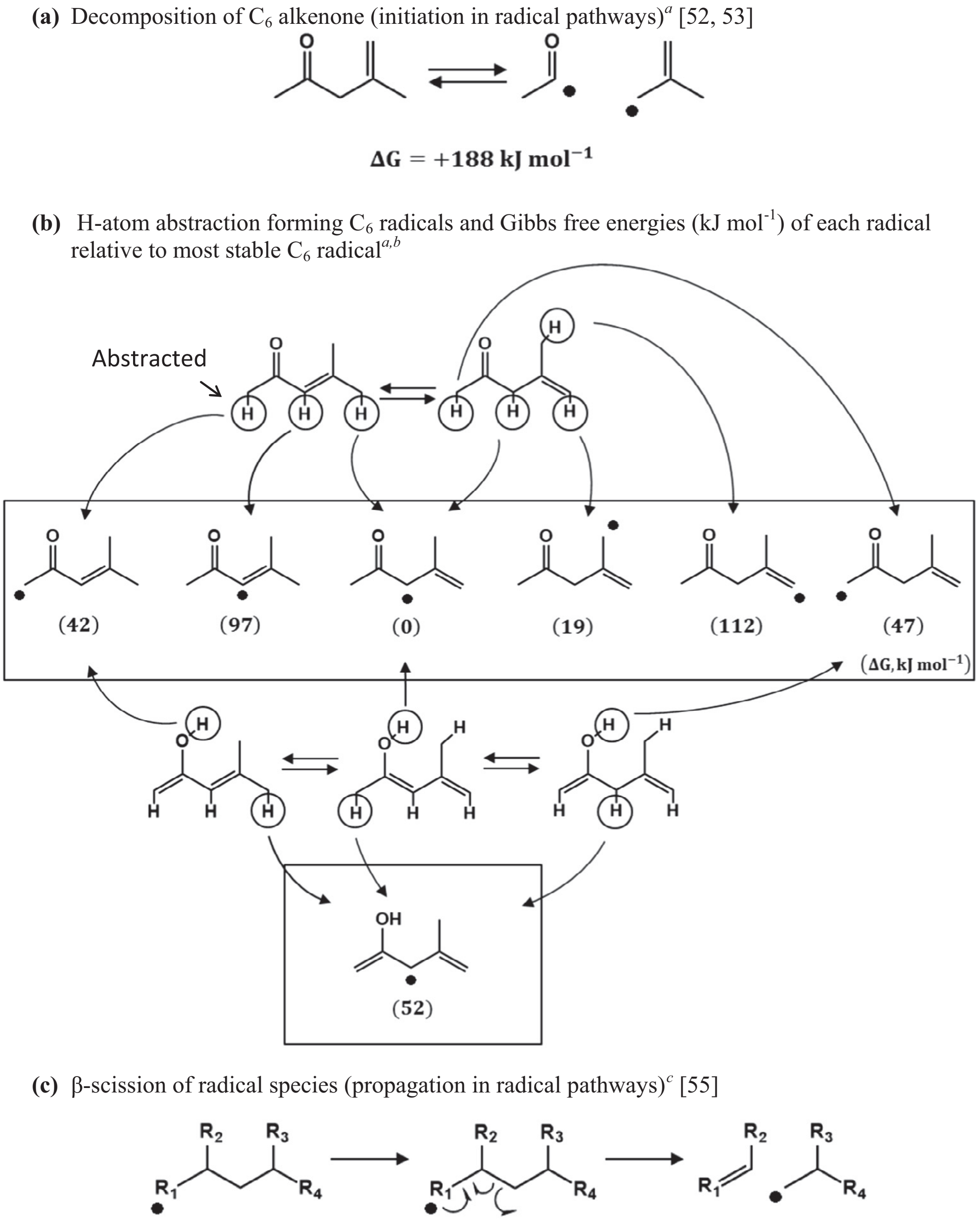
(a) Decomposition of C_6 alkenone (initiation in radical pathways)^a [52, 53]

$\Delta G = +188$ kJ mol^{-1}

(b) H-atom abstraction forming C_6 radicals and Gibbs free energies (kJ mol^{-1}) of each radical relative to most stable C_6 radical^{a,b}

(c) β-scission of radical species (propagation in radical pathways)^c [55]

Scheme 4. Radical formation reaction pathways. (a) Gibbs free energy differences between gaseous species and most stable gaseous radicals are provided (473 K, CCSD, AUG-cc-pVDZ; details in Section 2.3). Location of the unpaired electron is denoted with the black dot. (b) Open circles and arrows indicate which H-atom is abstracted from the C_6 species to form each radical (radicals are in boxes). Only distinct H-atoms in each C_6 molecule are explicitly shown. (c) Location of the unpaired electron is denoted with the black dot. Curved arrows indicate electron rearrangements that mediate β-scission events.

(17)) would be −85 kJ mol^{-1}, a value much larger than the estimated free energy stabilization of C_5-C_8 alkanes by MFI compared to FAU (−20 ± 2 to −40 ± 5 kJ mol^{-1} for C_5 to C_7, 473 K; [54]). If C_6 species do not initiate radical chains, then they must be involved in propagations events; this requires that radical initiation occurs via decomposition of a different species more susceptible to forming radical species, an event that occurs infrequently compared to the occurrence of propagation events during radical chain reactions.

C_6 alkenones or alkenols (Scheme 1) can donate a H-atom to radicals formed in initiation events, thus propagating the radical chain through the formation of a C_6 radical. The relative stabilities of plausible gaseous C_6 radicals that can form from MO and of their respective alkenols are shown in Scheme 4b, together with the H-atom abstraction steps that can form such radicals (473 K, CCSD, AUG-cc-pVDZ). These CCSD treatments show that four distinct C_6 radicals have relative free energies within 50 kJ mol^{-1} of the most stable C_6 radical, which is the free energy of the gaseous allylic isobutenyl radical and ketene (the products of radical-mediated β-scission) relative to the most stable C_6 radical (473 K, CCSD, AUG-cc-pVDZ). Of these four plausible C_6 radicals, one has the unpaired electron at the acyl C-atom and a terminal C—C double bond, a plausible structure to undergo β-scission reactions (Scheme 4c), which cleave C—C bonds at the β-position to the radical forming an allylic isobutenyl radical and ketene [55]; the latter readily reacts with H_2O to form acetic acid (a detected product).

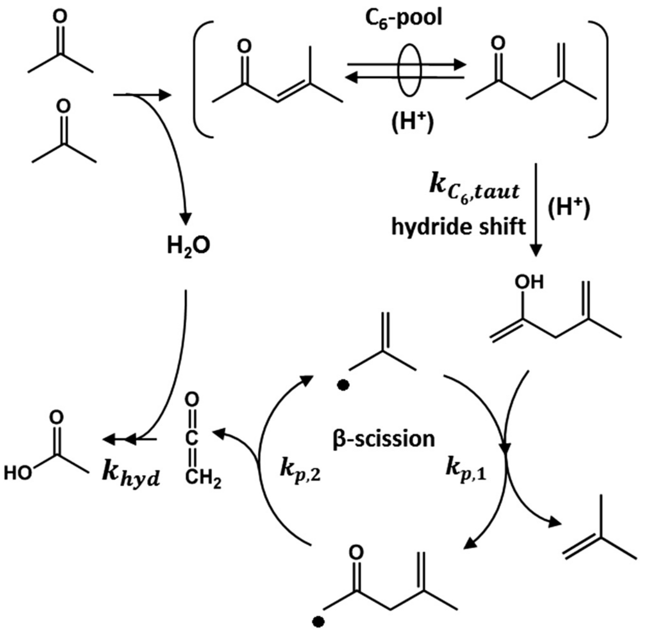

Scheme 5. Proposed elementary steps for isobutene and acetic acid formation from MO via the coupling of acid-catalyzed and free radical reactions. k_X denotes kinetic constants for forward steps. Quasi-equilibrated steps are indicated by an oval over double arrows. Location of the unpaired electron is denoted with a black filled circle.

The radical chain-reaction mechanism proposed here (Scheme 5) involves C_6 alkenols formed from the IMO-MO-DA equilibrated pool on protons via intramolecular hydride transfer. This C_6 alkenol donates a H-atom to an allylic isobutenyl radical forming isobutene and a C_6 radical (shown in Scheme 5) with the unpaired electron at the α-C of the acyl moiety. This radical undergoes β-scission forming an allylic isobutenyl radical and ketene, which converts to acetic acid (a detected product) via rapid hydrolysis with H_2O molecules formed stoichiometrically in acetone condensation. C_6 and C_4 radicals propagate through long radical chains [56], with each cycle forming one isobutene and one ketene (acetic acid) molecules, as shown in Scheme 5. Terminations occur via radical recombinations that re-form a C—C bond (the reverse of initiation reactions shown in Scheme 4a). Such reaction pathways are reminiscent of the classic Rice-Herzfeld radical mechanism [57]. The transition states that mediate these propagation cycles can be stabilized via van der Waals contacts with void walls; such interactions are most apparent within the MFI and BEA (Fig. 7), reflecting the similarity in void size and shape to that of the transition state. These rapid propagation events also require the proximate presence of protons to replenish the reactive C_6 alkenol intermediates that are used in the initiation steps in these cycles.

The reaction free energies for these radical propagation pathways (Scheme 5) relative to the free energy of the acetone condensation transition state [18] and the gaseous allylic isobutenyl radical are shown in Fig. 14 in the form of a reaction coordinate diagram (gaseous species, 473 K, CCSD, AUG-cc-pVDZ). The difference in free energy between the barrier for radical propagation

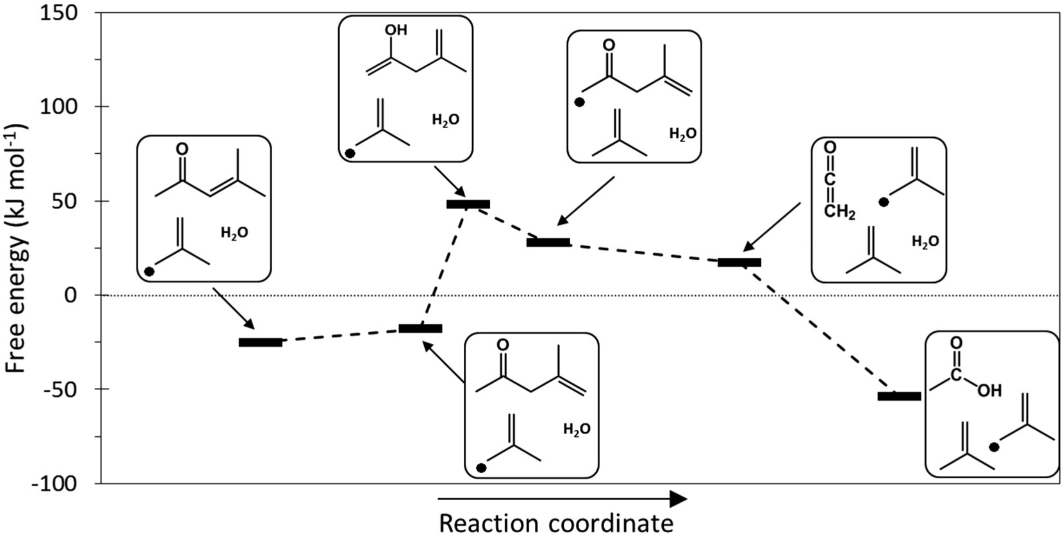

Fig. 14. Gibbs free energy diagram showing reaction energies for propagation of gaseous radicals in Scheme 4 relative to the acetone condensation transition state within MFI [18] and a gaseous allylic isobutenyl radical (473 K, 1 bar, AUG-cc-pVDZ, CCSD, Gaussian 09; details in Section 2.3). Location of the unpaired electron is denoted with a black filled circle.

compared to the barrier for acetone condensation [18] ($\Delta\Delta G_{\beta,MO}$, Eq. (17)) is 48 kJ mol^{-1} (Fig. 14), which does not include van der Waals stabilization interactions in these calculations for the radical propagation but were included in the free energy calculations of the activation barrier of acetone condensation [18]. Such interactions, as discussed above, are estimated to decrease the free energy of similar species (C_5-C_8 alkanes) in MFI by -20 ± 2 to -40 ± 5 kJ mol^{-1} (473 K; [54]), which would decrease the $\Delta\Delta G_{\beta,MO}$ value to nearly the measured value of -11 ± 10 kJ mol^{-1}. The theoretical treatments presented here are consistent with the formation of an unstable C_6 species, which is incorporated into radical propagation ultimately forming isobutene and acetic acid.

Pathways similar to those depicted in Scheme 5 have been proposed to describe the thermal decomposition of mesityl oxide to isobutene, methylbutenes, carbon monoxide, and methane at higher temperatures (685–763 K) [25]; the steps in Scheme 5 are also consistent with the ability of oxygenates to form radical species in the context of ketone photolyses and H-abstraction [52,53,58]. The lower temperatures at which these steps occur in the present study (473 K) reflect: (i) the proximate presence of protons that catalyze tautomerization of mesityl oxide to the respective alkenols (Scheme 1); and (ii) confining voids that stabilize initiation and propagation steps via van der Waals contacts. Similarly, confining voids, even without specific binding sites, also cause reactions to occur at much lower temperatures than their purely homogeneous analogs, especially as the size and shape of such voids becomes similar to those of the relevant transition states [27,28].

4. Conclusions

In this study, the elementary steps of isobutene (C_4) and acetic acid formation from acetone on solid Brønsted acid catalysts were identified by the combination of detailed kinetic measurements and rigorous mechanistic interpretations of rates and selectivities, taken together with theoretical estimations of free energies for reactive intermediates and radical species. At all reaction conditions studied, C_6 species were present at pseudo-steady-state concentrations, which allowed rigorous comparisons of C_4 selectivities, as C_4/MO product ratios, on a range of aluminosilicates by accounting for the effects of acetone conversion and acetone pressure. Here, we also show that C_4 species are derived from the β-scission of C_6 species, via two distinct reaction pathways: anhydrous (MO β-scission) and H_2O-mediated (DA β-scission). The addition of H_2O shifted the C_6-pool equilibrium concentrations leading to increased formation of C_4 species through the H_2O-mediated pathway and decreased catalyst deactivation. The addition of H_2O to MFI samples of different proton density further revealed that the two β-scission pathways have unique site requirements. The H_2O-mediated pathway requires only protons; whereas the rates of anhydrous β-scission pathways unexpectedly increased with decreasing proton density. The product selectivity dependence of the anhydrous pathway on proton density can only be explained by the kinetic coupling of protons, which form unstable C_6 alkenols, and nearby microporous volume, which stabilize transition states that mediate radical propagation cycles. Such pathways are supported by previous reports of the thermal decomposition of mesityl oxide and of proton-free microporous materials catalyzing reactions via confinement.

Acknowledgements

The authors acknowledge the financial support of BP, p.l.c. for this work as part of the BP Conversion Consortium (BP-XC^2); the technical discussions with Drs. John Shabaker and Glenn Sunley (BP, p.l.c.); and Dr. Raul Lobo (University of Delaware) and Drs. Nancy Artioli and Xiaoqin Zou (University of California, Berkeley) for the synthesis of the SIL-1 samples used. Computational facilities were provided by the Extreme Science and Engineering Discovery Environment (XSEDE), which is supported by the National Science Foundation (grant number: CHE-140066).

Notes

The authors declare no competing financial interest.

Appendix A. Supplementary material

Supplementary data associated with this article can be found, in the online version, at https://doi.org/10.1016/j.jcat.2018.01.032.

References

[1] D. Kubička, O. Kikhtyanin, Opportunities for zeolites in biomass upgrading-lessons from the refining and petrochemical industry, Catal. Today 243 (2015) 10–22.
[2] D.M. Alonso, J.Q. Bond, J.A. Dumesic, Catalytic conversion of biomass to biofuels, Green Chem. 12 (2010) 1493–1513.
[3] B.H. Shanks, Conversion of biorenewables feedstocks: new challenges in heterogeneous catalysis, Ind. Eng. Chem. Res. 49 (21) (2010) 10212–10217.
[4] J. Sun, Y. Wang, Recent advances in catalytic conversion of ethanol to chemicals, ACS Catal. 4 (4) (2014) 369–453.
[5] R.A. Sheldon, Green and sustainable manufacture of chemicals from biomass: state of the art, Green Chem. 16 (3) (2014) 950–963.
[6] T.N. Pham et al., Ketonization of carboxylic acids: mechanisms, catalysts, and implications for biomass conversion, ACS Catal. 3 (11) (2013) 2456–2473.
[7] S. Wang, E. Iglesia, Experimental and theoretical assessment of the mechanism and site requirements for ketonization of carboxylic acids on oxides, J. Catal. 34 (2017) 183–206.
[8] C.A. Gaertner et al., Catalytic coupling of carboxylic acids by ketonization as a processing step in biomass conversion, J. Catal. 266 (1) (2009) 71–78.
[9] M. Demorest, D. Mooberry, J.D. Danforth, Decomposition of ketones and fatty acids by silica-alumina composites, Ind. Eng. Chem. Res. 43 (11) (1951) 2569–2572.
[10] A.N. Shuikin, et al., Conversion of acetone to isobutylene on a silica-tungsten catalyst, Pet. Chem. U.S.S.R. 17(3) (1977) 173–180.
[11] G. Hutchings et al., Acetone conversion to isobutene in high selectivity using zeolite β catalyst, Catal. Lett. 21 (1–2) (1993) 49–53.
[12] L. Kubelková et al., Acetone conversion and deactivation of zeolites, in: P.A. Jacobs, R.A.V. Santen (Eds.), Studies in Surface Science and Catalysis, Elsevier, 1989, pp. 1203–1212.
[13] J. Cejka, J. Pavel, Influence of water on activity, selectivity and deactivation of zeolites in acetone transformation, Collect. Czech. Chem. Commun. 54 (11) (1989) 2998–3002.
[14] T. Tago et al., Selective production of isobutylene from acetone over alkali metal ion-exchanged BEA zeolites, Catal. Today 164 (1) (2011) 158–162.
[15] T. Tago et al., Selective synthesis for light olefins from acetone over ZSM-5 zeolites with nano- and macro-crystal sizes, Appl. Catal. A 403 (1–2) (2011) 183–191.
[16] M. Sarazen, E. Doskocil, E. Iglesia, Catalysis on solid acids: mechanism and catalyst descriptors in oligomerization reactions of light alkenes, J. Catal. 344 (2016) 553.
[17] A. Gumidyala, T. Sooknoi, S. Crossley, Selective ketonization of acetic acid over HZSM-5: the importance of acyl species and the influence of water, J. Catal. 340 (2016) 76–84.
[18] S. Herrmann, E. Iglesia, Elementary steps in acetone condensation reactions catalyzed by aluminosilicates with diverse void structures, J. Catal. 346 (2017) 134–153.
[19] A. Panov, J.J. Fripiat, An infrared spectroscopic study of acetone and mesityl oxide adsorption on acid catalyst, Langmuir 14 (14) (1998) 3788–3796.
[20] G.S. Salvapati, K.V. Ramanamurty, M. Janardanarao, Selective catalytic self-condensation of acetone, J. Mol. Catal. 54 (1) (1989) 9–30.
[21] C.D. Chang, A.J. Silvestri, The conversion of methanol and other o-compounds to hydrocarbons over zeolite catalysts, J. Catal. 259 (47) (1977) 249–259.
[22] S. McAllister, W. Bailey, C. Bouton, The catalyzed cleavage of diacetone alcohol and other ketols and unsaturated ketones, J. Am. Chem. Soc. 62 (11) (1940) 3210–3215.
[23] A. Panov, J. Fripiat, Poisoning of aldol condensation reaction with H_2O on acid catalysts, Catal. Lett. 57 (1–2) (1999) 25–32.
[24] C.O. Veloso, J.L.F. Monteiro, E.F. Sousa-Aguiar, Aldol condensation of acetone over alkali cation exchanged zeolites, Stud. Surf. Sci. Catal. 84 (1994) 1913–1920.
[25] N.J. Daly, M.F. Gilligan, Thermal reactions of mesityl oxide, Aust. J. Chem. 24 (5) (1971) 955–960.

[26] B. Boekfa et al., Adsorption and tautomerization reaction of acetone on acidic zeolites: the confinement effect in different types of zeolites, J. Phys. Chem. C 114 (35) (2010) 15061–15067.
[27] N. Artioli, R.F. Lobo, E. Iglesia, Catalysis by confinement: Enthalpic stabilization of NO oxidation transition states by micropororous and mesoporous siliceous materials, J. Phys. Chem. C 117 (40) (2013) 20666–20674.
[28] R.M. Dessau, Catalysis of diels-alder reactions by zeolites, J. Chem. Soc., Chem. Commun. 331 (1986) 1167–1168.
[29] E.L. First et al., Computational characterization of zeolite porous networks: an automated approach, Phys. Chem. Chem. Phys.: PCCP 13 (38) (2011) 17339–17358.
[30] S.A.I. Barri, D. Young, Crystalline zincosilicate, in: E.P. Office (Ed.), 1984, Google Patents: Great Britain.
[31] W.J. Ball, S.A.I. Barri, D. Young, Improved method of preparing crystalline aluminosilicates, in: E.P. Office (Ed.), 1986, Great Britain.
[32] A.J. Jones et al., Acid strength and solvation in catalysis by MFI zeolites and effects of the identity, concentration and location of framework heteroatoms, J. Catal. 312 (2014) 58–68.
[33] C. Baerlocher, L.B. McCusker. Database of Zeolite Structures. February 6, 2016]; Available from: http://www.iza-structure.org/databases/.
[34] J. Cížek, Advances in chemical physics, in: P.C. Hariharan (Ed.), vol. 14, 1969, Wiley Interscience, New York.
[35] G.D.I. Purvis, R.J. Bartlett, A full coupled-cluster singles and doubles model – the inclusion of disconnected triples, J. Chem. Phys. 76 (1982) 1910–1918.
[36] G.E. Scuseria, C.L. Janssen, H.F. Schaefer III, An efficient reformulation of the closed-shell coupled cluster single and double excitation (CCSD) equations, J. Chem. Phys. 89 (1988) 7382–7387.
[37] G.E. Scuseria, H.F. Schaefer III, Is coupled cluster singles and doubles (CCSD) more computationally intensive than quadratic configuration-interaction (QCISD)?, J Chem. Phys. 90 (1989) 3700–3703.
[38] R.A. Kendall, T.H. Dunning Jr., R.J. Harrison, Electron affinities of the first-row atoms revisited. Systematic basis sets and wave functions, J. Chem. Phys. 96 (1992) 6796–6806.
[39] T.H. Dunning Jr., Gaussian basis sets for use in correlated molecular calculations. I. The atoms boron through neon and hydrogen, J. Chem. Phys. 90 (1989) 1007–1023.
[40] D.E. Woon, T.H. Dunning Jr., Gaussian-basis sets for use in correlated molecular calculations. 3. The atoms aluminum through argon, J. Chem. Phys. 98 (1993) 1358–1371.
[41] M.J. Frisch et al., Gaussian 09, Revision D.01, Gaussian Inc, Wallingford, CT, USA, 2009.
[42] J.W. Lee, J.B. Butt, D.M. Downing, Kinetic, transport, and deactivation rate interactions on steady state and transient responses in heterogeneous catalysis, AIChE J. 24 (2) (1978) 212–222.
[43] E.E. Wolf, E.E. Petersen, On the kinetics of self-poisoning catalytic reactions, J. Catal. 47 (1) (1977) 28–32.
[44] A. Zecchina et al., IR spectroscopy of neutral and ionic hydrogen-bonded complexes formed upon interaction of CH_3OH, C_2H_5OH, $(CH_3)_2O$, $(C_2H_5)_2O$ and C_4H_8O with H-Y, H-ZSM-5 and H-mordenite: comparison with analogous adducts formed on the H-Nafion superacidic membrane, J. Chem. Soc., Faraday Trans. 92 (23) (1996) 4863–4875.
[45] C. Pazé et al., Acidic properties of H-β zeolite as probed by bases with proton affinity in the 118–204 kcal mol-1 range: a FTIR investigation, J. Phys. Chem. B 101 (24) (1997) 4740–4751.
[46] O. Levenspiel, Experimental search for a simple rate equation to describe deactivating porous catalyst particles, J. Catal. 25 (1972) 265–272.
[47] H. Konno et al., Characterization and catalytic performance of modified nano-scale ZSM-5 for the acetone-to-olefins reaction, Appl. Catal. A 475 (2014) 127–133.
[48] T. Masuda, et al., Process for producing isobutylene from acetone. 2010, Google Patents.
[49] P. Jiru, Catalytic zeolite for acetone conversion to isobutene. 1986, JIRU P (JIRU-Individual).
[50] H. Eyring, The activated complex in chemical reactions, J. Chem. Phys. 3 (2) (1935) 107–115.
[51] M.G. Evans, M. Polanyi, Some applications of the transition state method to the calculation of reaction velocities, especially in solution, Trans. Faraday Soc. 31 (1935) 875–894.
[52] M.J. Gibian, R.C. Corley, Organic radical-radical reactions, disproportionation vs. combination, Chem. Rev. 73 (5) (1973) 441–454.
[53] H. Fischer, H. Paul, Rate constants for some prototype radical reactions in liquids by kinetic electron spin resonance, Acc. Chem. Res. 20 (5) (1987) 200–206.
[54] B.A. De Moor et al., Adsorption of C2–C8 n-alkanes in zeolites, J. Phys. Chem. C 115 (2011) 1204–1219.
[55] K.E. Gilbert, J.J. Gajewski, Coal liquefaction model studies: free radical chain decomposition of diphenylpropane, dibenzyl ether, and phenethyl phenyl ether via b-scission reactions, J. Organ. Chem. 47 (25) (1982) 4899–4902.
[56] G.R. Gavalas, The long chain approximation in free radical reaction systems, Chem. Eng. Sci. 3 (21) (1966) 133–141.
[57] F.O. Rice, K.F. Herzfeld, Thermal decomposition of organic compounds from the standpoint of free radicals. VI. The mechanism of some chain reactions, J. Am. Chem. Soc. 56 (4) (1934) 285–289.
[58] E. Diaz, M.E. Sad, E. Iglesia, Homogeneous oxidation reactions of propanediols at low temperatures, ChemSusChem 3 (9) (2010) 1063–1070.